Thiourea-assisted nitrogen and sulfur dual-doped carbon nanofibers for enhanced supercapacitive energy storage

Burcu Üstün[1], Hamide Aydın[2], Serkan Naci Koç[1], and Ümran Kurtan[3,*] (ID)

[1] *Department of Chemical Engineering, İstanbul University-Cerrahpaşa, 34500 Istanbul, Turkey*

[2] *Department of Chemistry, İstanbul University-Cerrahpaşa, 34500 Istanbul, Turkey*

[3] *Department of Materials and Materials Processing Technologies, Vocational School of Technical Sciences, İstanbul University-Cerrahpaşa, 34500 Istanbul, Turkey*

ABSTRACT

Herein, using thiourea is a simple and effective approach to produce the unique structure constructed by N and S dual-doped carbon nanofibers. The surface porosity is optimized by changing the thiourea amount in the polymer solution. The optimized N/S-CNF5, which the weight percentage of thiourea to polyacrylonitrile is 5, has a high specific surface area ($144.2 \ m^2 \ g^{-1}$) and rich content of heteroatoms (N-4.66 at% and S-0.11 at.%), respectively. Because of these unique features, N/S-CNF5 demonstrates a large gravimetric-specific capacitance ($312 \ F \ g^{-1}$ at $10 \ mV \ s^{-1}$ and $225 \ F \ g^{-1}$ at $1 \ A \ g^{-1}$). The N/S-CNF5 electrode represents in the two-electrode system with a high specific capacitance of $160 \ F \ g^{-1}$ at $1 \ A \ g^{-1}$ and shows a remarkable rate of performance (87.5% retention) even at $5 \ A \ g^{-1}$. Moreover, the symmetrical supercapacitor device (N/S-CNF5//N/S-CNF5) delivers specific energy of as high as $5.5 \ Wh \ kg^{-1}$ with a specific power of $250 \ W \ kg^{-1}$. Also, the device's cycling ability is 78.3% even after 30 000 cycles at $1 \ A \ g^{-1}$. This strategy can be feasible to explore more dual heteroatom-doped carbon nanomaterials for a wide range of electrochemical applications.

1 Introduction

Energy is one of the crucial issues in the past years due to the depletion of fossil fuels and environmental pollution, and thus, great efforts have been dedicated to improving energy storage devices, including fuel cells, batteries, solar cells, capacitors, and supercapacitors (SCs) [1–6]. Among them, SCs represent a potential electrochemical energy storage equipment. The most significant feature of SCs is that they have higher specific power than batteries owing to the electrochemical charge accumulation at the electrical double layer and the presence of redox reactions

---

Address correspondence to E-mail: umran.kurtan@iuc.edu.tr

resulting from surface functionalities [6–8]. Unfortunately, low specific energy limits the development of energy storage in SCs and thus can be improved in order to make them efficient for hybrid power sources for applications like wearable electronics, electric vehicles, or medical sensors [8, 9]. Porous carbon nanofibers (CNFs) have been widely used as electrode materials in SCs owing to their stable physicochemical properties, high specific surface area, and low cost [10–13]. However, they have some drawbacks, such as low electrical conductivity and insufficient textural characteristics, which are so essential for supercapacitive performance; thus, much interest has been given to improving their properties. The optimized pore structure is required to obtain the high specific capacitance since CNFs store and release energy via ions adsorption–desorption on the surface of the electroactive sites. Adding some polymers such as polyvinylpyrrolidone (PVP), polyvinyl alcohol (PVA), polyaniline (PANI), and polymethylmethacrylate (PMMA) into polyacrylonitrile (PAN) polymer provides a higher surface area with a well-developed pore structure, increasing the electrochemical performance of SCs [11, 14–17]. Another efficient strategy is introducing heteroatom (i.e., N, S, B, or F) dopants into the carbon matrix for designing SC electrodes for enhanced energy storage performance [12, 18–21]. Besides, heteroatom dopants, especially nitrogen and sulfur, into CNFs can increase not only their wettability due to their electron donor properties but also contribute an additional pseudocapacitive effect by reversible faradic reactions [22–27].

Nitrogen doping is generally used to synthesize electron-rich CNFs with highly porous structures [17, 28]. For example, Tahir et al. synthesized g-C_3N_4 nanofibers using melamine and found the specific capacitance of electrode as 263.75 F g^{-1} at 1 A g^{-1} [8]. In another work, CNF was fabricated from a mixture of PAN with 5% melamine by the electrospinning, and the specific capacitance was as 435.47 mAh g^{-1} at 20 mA g^{-1} [29]. Sulfur has also similar electronegativity with carbon, and it has important contributions such as tuning electronic properties, polarizing electron pairs, forming charge sites, and significantly increases the surface electron affinity of the electrolyte. These properties make sulfur attractive as heteroatom for SCs [18]. Hasekawa et al. prepared sulfur-activated carbon with high surface area and high conductivity with a specific

capacitance of 206 F g^{-1} at 1 A g^{-1} [30]. Nazish Parveen et al. produced S-doped graphene with a high specific capacitance of 320 F g^{-1} at 3 A g^{-1} and Zong et al. found the specific capacity of N and S dual-doped CNF as 280.1 F g^{-1} at 1 A g^{-1} [31, 32].

The enhancement in capacitance was still limited, and thus, the dual heteroatom doping has been investigated to find a better supercapacitive performance. For this purpose, thiourea is a good and low-cost alternative source for both nitrogen and sulfur doping and has been investigated in some recent works. For instance, Xie et al. used thiourea and phenolic resin as a source of both nitrogen and sulfur, and a carbon source, respectively. The N/S co-doped mesoporous electrode was synthesized and the specific capacitance of the N/S-MC-6// N/S-MC-6 device was 125 F g^{-1} at 0.5 A g^{-1} [33]. Lei et al. fabricated N/S dual-doped carbon fibers (NSCF) by using bacterial cellulose as the carbon source in saturated thiourea aqueous solution with an absorption-swelling strategy. The electrode had a specific capacitance of 202 F g^{-1} and the NSCF based cell was 80 F g^{-1} at 0.5 A g^{-1} [34]. Wang et al. produced porous carbon nanosheets from melamine/formaldehyde/thiourea (MFT) resins followed by pyrolysis. The specific capacitance of N/S co-doped C-MFT-2 cell was 80 F g^{-1} at 1 A g^{-1} [35]. Inspired by these previous studies, thiourea was utilized as a source of both nitrogen and sulfur doping for the preparation of mesoporous CNF. As we know, thiourea has not been studied so far by the electrospinning strategy for N/S doping.

In this paper, newly N and S dual-doped hierarchical porous CNFs architecture was formed via a one-pot synthesis of electrospinning of polyacrylonitrile (PAN) incorporated with thiourea as a source of both nitrogen and sulfur after thermal treatment. The results demonstrated that the as-fabricated N and S dual-doped CNFs (N/S-CNFs) represent great potential as electrodes for SCs with remarkable electrochemical performance, that is, a relatively large specific capacitance, high specific energy, excellent rate capability, and cycle stability.

2 Materials and methods

2.1 Materials

Polyacrylonitrile (PAN, $M_w = 150,000$) and poly(methylmethacrylate) (PMMA, $M_w = 120,000$) were obtained from Sigma Aldrich and Alfa Aesar,

respectively. Dimethylformamide (DMF) was obtained from Merck. Thiourea was purchased from Labshop41.

2.2 The preparation of N and S dual-doped carbon nanofibers

1.4 g of polyacrylonitrile (PAN) with 0.6 g of polymethyl methacrylate (PMMA) and different amounts of thiourea (0 g, 0.035 g, 0.07 g, and 0.14 g) were added into 18 g DMF to get 10 wt% polymer solution. Then the solution was mixed at 70 °C overnight with a magnetic stirrer to obtain a homogeneous solution. Subsequently, the as-spun nanofibers were fabricated by the electrospinning process. The parameters were set as 20 cm distance to collector, 1 ml h^{-1} feeding ratio, and applied voltage was set to 18 kV. Finally, the as-spun nanofibers were preoxidized at 280 °C for 2 h and then carbonized at 800 °C for 2 h under an N$_2$ flow with a heating rate of 5 °C min^{-1}. The resultant samples were abbreviated as CNF, N/S-CNF2.5, N/S-CNF5, and N/S-CNF10, where the numbers 2.5, 5, and 10 represent the weight percentage of thiourea to polyacrylonitrile.

2.3 Structural characterization

SEM and TEM images were obtained on field emission scanning electron microscopy (SEM; Zeiss Sigma 300, 3 kV) and transmission electron microscopy (TEM; Hitachi HT7700), respectively. Raman analysis was recorded at ambient temperature on a WITech Alpha 300R Raman spectrometer with an air-cooled DPSS laser up to 100 mW at 532 nm. The specific surface area and porosity of the dual-doped CNFs were examined by nitrogen adsorption/desorption isotherms by a Micromeritics at 76 K. The surface area and pore size distribution of the dual-doped CNFs were determined by Brunauer–Emmett–Teller (BET) procedure. The total pore volume was assessed by BJH (Barrett–Joyner–Halenda) procedure. X-ray photoelectron spectroscopy (XPS) analysis were conducted with K-Alpha XPS system (Thermo Fisher Scientific) with an Al Kα X-ray source (Fig. 1).

2.4 Electrochemical tests in a three-electrode system

Electrochemical measurements were performed using GAMRY Reference 3000 for two- and three-electrode systems. In this system, a binder-free CNFs were used as the working, Ag/AgCl as the reference, and Pt as the counter electrode. CNFs were placed between two nickel foams (flag-like, 1 × 1 cm^2 area) and pressed under pressure. 6 M KOH was used as the electrolyte. The electrochemical performances of the CNFs were evaluated by cyclic voltammetry (CV) and galvanic charge–discharge (GCD) techniques.

The gravimetric-specific capacitance (C$_S$) of the CNF electrode materials from CV and GCD curves can be calculated from the Eq. 1:

$$C_S = \frac{1}{mv\Delta V} \int_{V_1}^{V_2} IdV, \quad C_S = I \times \Delta t/(m\Delta v), \tag{1}$$

where I, Δt, m, v, and ΔV are current, discharging time, the mass of the active material, scan rate, and potential window, respectively.

2.5 Electrochemical tests in a two-electrode system

In two-electrode system, the SC cell was assembled by compressing CR2032 button-type cells with an electrical battery closing machine. Two pieces of CNF electrodes (10 mm diameter) and a piece of Whatman separator (19 mm diameter) were cut. Then, they were placed into the button-type CR2032 cell as electrode/separator/electrode in 6 M KOH, respectively. The CV curves were obtained in the potential range of 0-1 V at several sweeping rates. A BST8-MA 8-channel battery analyzer (0.02-10 mA, 5V, MTI Corp.) device was used for GCD tests. The GCD tests were recorded in the potential range of 0–1 V at different current densities. 30 000 charge–discharge cycles were performed on SC cells, and the capacity, the specific energy, the specific power, and the cycle stability of the SC cells were calculated with the Eqs. 2 and 3. The electrochemical impedance spectroscopy (EIS) analysis was implemented in the frequency range of 0.01 Hz–100 kHz. The specific capacitance for the single electrode (C$_{sp}$) was calculated via Eq. (2).

$$C_{electrode} = 2I \times \Delta t/(m\Delta V) \tag{2}$$

where I is the discharge current, Δt is the discharge time, m is the mass of the single electrode, and ΔV is the voltage range, respectively.

$$C_{cell} = C_{electrode}/4,$$
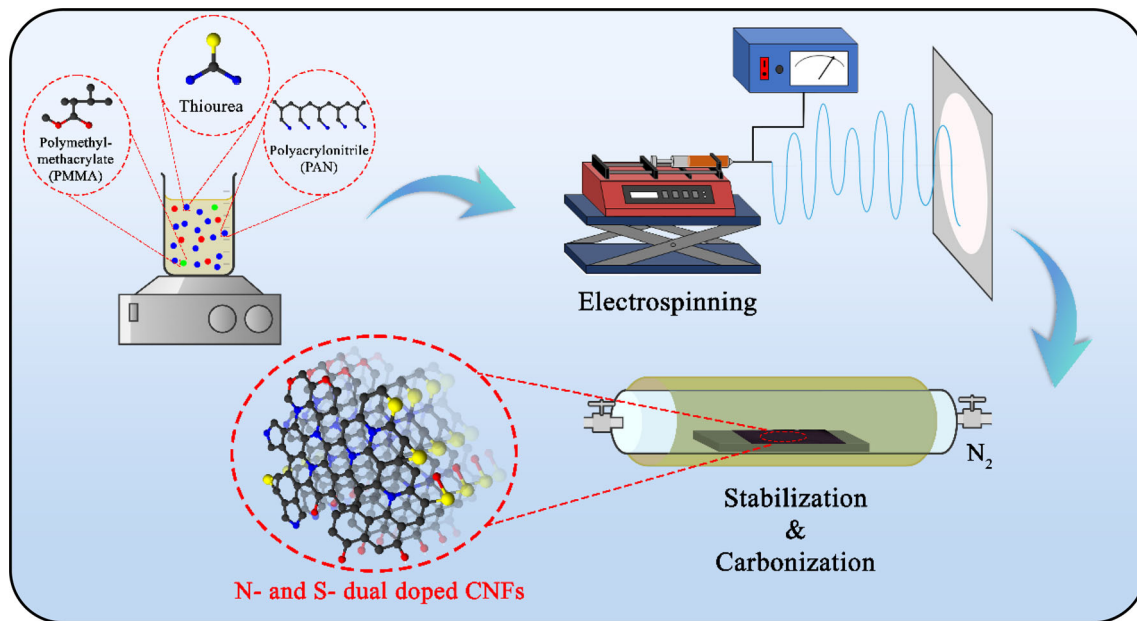
where C_{cell} is the specific capacitance of a cell

Fig. 1 Schematic illustration of the fabrication of N/S-CNFs

$$E = C_{cell}\,\Delta V^2 / (2 \times 3.6), \tag{3}$$

$$P = 3600 \times E / \Delta t, \tag{4}$$

where P and E are the specific power (W kg^{-1}) and specific energy (Wh kg^{-1}), respectively.

3 Results and discussion

3.1 Characterization of samples

SEM images were recorded to investigate the microscopic morphologies and internal porosities of the CNFs prepared after carbonization by thiourea removal. The SEM images of the nanofibers were taken at different magnifications of 5 μm as displayed in Fig. 2a. Figure 2a–d show the representative fibrous structure of CNF, N/S-CNF2.5, N/S-CNF5, and N/S-CNF10, respectively, revealing the successful production of a network-like porous nature. The SEM images indicated that uniform nanofibers were synthesized with the same diameter, homogeneous distribution, and regular morphology. No cracks (defects), stacks, or branches in the fibers were observed. The diameters of the prepared CNF, N/S-CNF2.5, N/S-CNF5, and N/S-CNF10 were estimated around 270 nm, 330 nm, 380 nm, and 440 nm, respectively. These results show that fiber diameters increase with the increase in the amount of thiourea.

Figure 3a shows the SEM image of the N/S-CNF5 with a high-resolution (1 μm, inset 200 nm). Adding thiourea caused the formation of uniform fibers with larger diameters without any agglomeration and supported the preservation of the fibrous and the porous structure. TEM images exhibit further information related to the morphology and structures of CNFs. In Fig. 3b and Fig. 3c, it was seen that N/S-CNF5 had a well-developed fiber structure and micropore structure. The EDX results and the elemental mapping of the N/S-CNF5 electrode are shown in Fig. 4. From EDX analysis, it is possible to get the elemental combination and nanocomposite purity.

The EDX results (Fig. 4a) show the corresponding element contents for the prepared N/S-CNF5; C (82.90 wt%), O (4.60 wt%), N (12.20 wt%), and S (0.30 wt%). The elemental mappings in Fig. 4b–e verify the homogenous distribution of C, O, N, and S elements on the N/S-CNF5. Consequently, characterization results showed that the tunable amount of N and S elements was successfully doped onto CNFs [36].

BET analysis was performed to investigate the porosity parameters of CNFs (Fig. 5a). The isotherms of samples show a hysteresis loop which is the leading property of porous samples. The electrochemically accessible surface area is directly concerned with the performance of any SC. The total BET
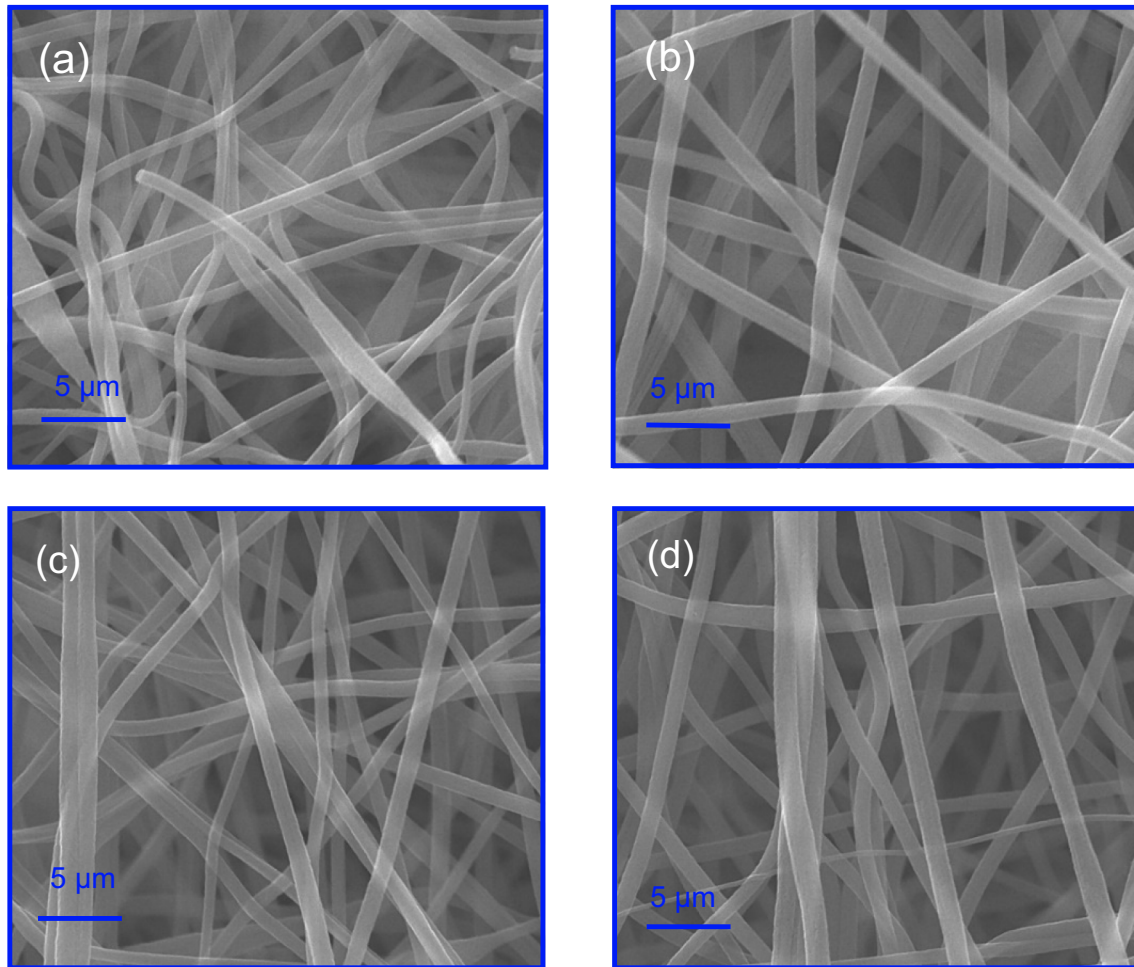
Fig. 2 SEM images of **a** CNF, **b** N/S-CNF2.5, **c** N/S-CNF5, and **d** N/S-CNF10

surface areas for CNF, N/S-CNF2.5, N/S-CNF5, and N/S-CNF10 were 62.8, 113.5, 144.2, and 33.1 $m^2\ g^{-1}$, respectively (Table 1). Compared to the pure CNF, N/S-CNF5 not only had a remarkably increased surface area but also showed a significant improvement in total pore volume. This is because the decomposition of large amounts of organic products coming from thiourea and PMMA causes the generation of more pores.

The pore size distribution graphs of CNF, N/S-CNF2.5, N/S-CNF5, and N/S-CNF10 are shown in Fig. 5b. It is well known that the introduction of micropores is significant for charge storage, whereas the existence of small mesopores is critical for ion transport. N/S-CNF5 had a narrow micropore size distribution (0.65–2 nm) and a broad mesopore size distribution (2–10 nm). The micropore size was close to the size of K + ions (0.33 nm), which contributed to the capacitive performance. The pore volume and

the specific surface area increased significantly with the increase of thiourea. But too high an amount of thiourea addition caused the decrease in specific surface area for N/S-CNF10 electrode due to the stacking of carbon layers and will influence their electrochemical results. Among thiourea-doped nanofibers, N/S-CNF5 had the largest total pore volume with high surface area and better mesoporosity and microporosity which show a promising electrode material for SCs [37, 38].

The carbon natures of synthesized samples were analyzed through Raman spectroscopy (Fig. S1). The Raman specific D-band at 1332 cm^{-1} corresponded to the non-crystalline part, whereas the other typical G-band at 1567 cm^{-1} corresponded to the crystalline part. The intensity ratio of D-band to G-band (I_D/I_G) for pure CNF was about 1, while the one for N/S-CNF2.5, N/S-CNF5, and N/S-CNF10 was about 0.91, 0.88, and 0.89, respectively. The value of I_D/I_G
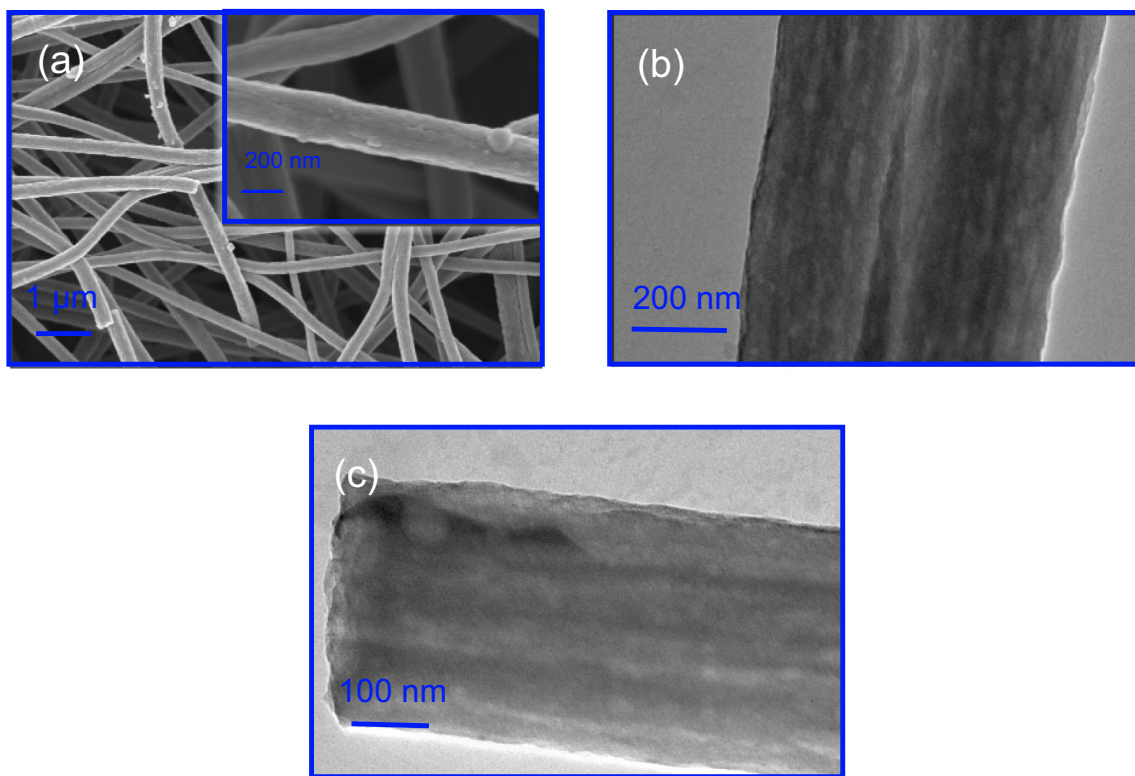
Fig. 3 a SEM images of the N/S-CNF5 at low magnification and **b**, **c** TEM images of the N/S-CNF5

reduced from 1 to 0.88 as the concentration of added thiourea enhanced. Among them, N/S-CNF5 had the lowest I_D/I_G value, which means its carbon structure possesses the highest graphitization degree. This is probably due to its good carbonization and high content of dual doping (nitrogen and sulfur), and all these results confirm the formation of carbon structure successfully. Heteroatom doping both increases the electrical conductivity and induces the pseudo-capacitive effect in aqueous electrolytes, thus improving the electrochemical performance.

The detailed element compositions and electronic states in the N/S-CNF5 were established by XPS. The XPS spectra displayed that N/S-CNF5 was essentially composed of C, N, O, and S (Fig. 6a). In Fig. 6a, four peaks of C 1 s ($\sim$ 284.9 eV), N1s ($\sim$ 399.8 eV), O1s ($\sim$ 532.7 eV), and S2p ($\sim$ 154 eV) coexisted in the survey spectra [39]. The atomic percentages of C, O, N, and S in N/S-CNF5 were 82.45%, 12.78%, 4.66%, and 0.11%, respectively (Table 2). The high-resolution spectrum of C 1 s can be separated into three peaks at around 284.8 eV, 286 eV, and 288.5 eV ascribed to the C–C, O–C–O/C=O, and O–C=O, respectively [40] (Fig. 6b). Moreover, the deconvolution of the O 1 s spectra of N/S-CNF5 showed three

components of oxygen species centered in the region of 530.8 eV, 532.6 eV, and 533.5 eV corresponding to C=O groups, C–OH/C–O–C groups, and moisture, respectively (Fig. 6c) [40–42]. The high-resolution spectrum of N 1 s represented three peaks with binding energy values of 398 eV, 400.8 eV, and 404.8 eV for the pyridinic-N, pyrrolic-N, and oxidized-N, respectively (Fig. 6d) [38, 43, 44]. Deconvolution of the high-resolution S 2p spectrum exhibited three distinct peaks, corresponding to the $2p_{3/2}$, $2p_{1/2}$, and/or SO_x band located at about 163.6 eV, 164.7 eV, and 168.4 eV, respectively (Fig. 6e) [45, 46]. These heteroatoms doping in carbon framework can allow the distribution of electrolyte into the pores of electrode to enhance the capacitance performance [35].

3.2 Electrochemical performance in a three-electrode system

Figure 7a shows the comparison CV graphs of electrochemical activities of nanofibers evaluated by three-electrode experiments at the scan rate of 100 mV s^{-1}. The CV curves of all materials had an approximately rectangular shape which indicates the
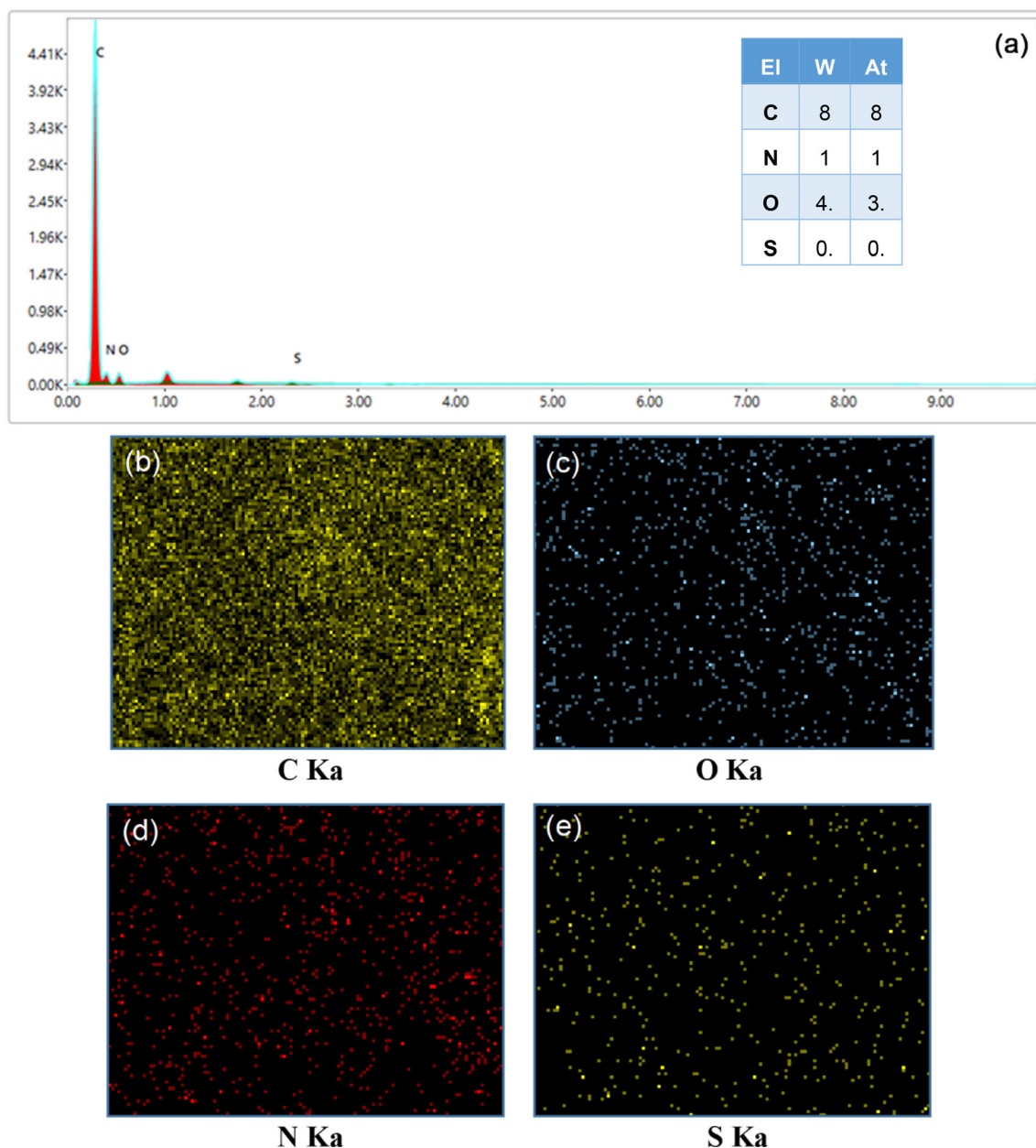
El	W	At
C	8	8
N	1	1
O	4.	3.
S	0.	0.

Fig. 4 **a** EDX spectrum and **b–e** elemental mapping images of C, O, N, and S elements in N/S-CNF5

main nature of electrochemical double-layer capacitor (EDLC), but the CV graph of N/S-CNFs presents a slight twist, which means a pseudocapacitive behavior resulting from N/S dual-doping effect. The CV graphs of N/S-CNF2.5, N/S-CNF5, and N/S-CNF10 with relatively large surface area demonstrated much higher capacitance, probably due to the improved properties like large surface area, optimized pathway for electrolyte, and a well crystalline structure, and so on. The CV curve of N/S-CNF5 had the largest integrated area demonstrating the best capacitance. CNF, N/S-CNF2.5, N/S-CNF5, and N/S-CNF10 electrodes exhibited specific capacitance values of 232, 259, 288, and 250 F g^{-1} at 100 mV s^{-1}, respectively. The area under the CV curves increased gradually with increasing the amount of thiourea and reached a maximum capacitive charging activity at thiourea content of 5 wt%. However, when the thiourea content was 10 wt%, the integrated area within the CV curve decreased. It can be caused by the diminished electrochemical active surface area with the loss of functional groups.
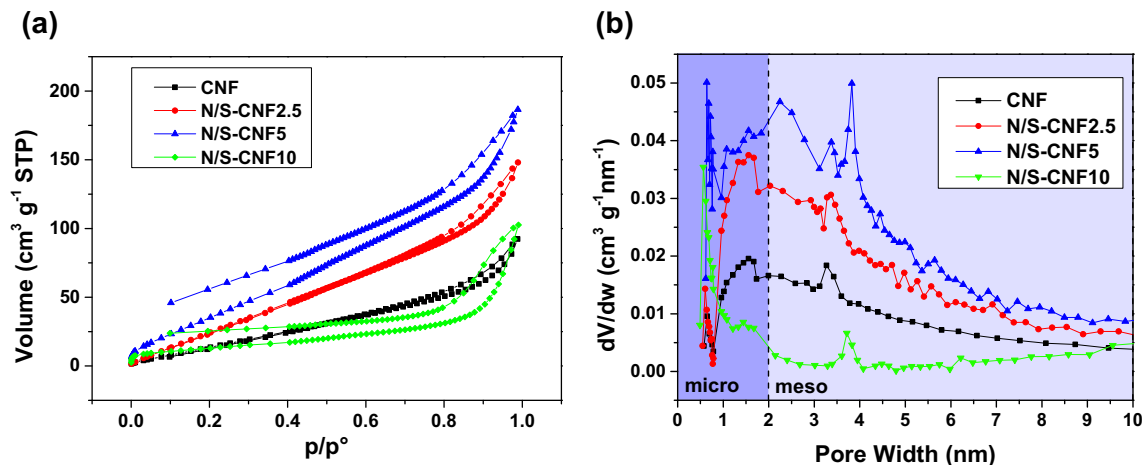
(a)

(b)

Fig. 5 a Nitrogen adsorption/desorption isotherms of CNF, N/S-CNF2.5, N/S-CNF5, and N/S-CNF10 and **b** pore size distribution curves based on the BJH model

The GCD analysis was also performed to evaluate the electrochemical activity of the samples. The GCD plots of N/S-CNF2.5, N/S-CNF5, and N/S-CNF10 had a prolonged discharge time at 1 A g^{-1} (Fig. 7b). The specific capacitances of all samples at several current densities are shown in Fig. 7c. Clearly, the N/S-CNF5 exhibited maximum discharge time at 1 A g^{-1}. N/S-CNF5 was a higher gravimetric-specific capacitance of 225 F g^{-1}, which is markedly higher than that of pure CNF (154 F g^{-1}), N/S-CNF2.5 (198 F g^{-1}), and N/S-CNF10 (181 F g^{-1}). The remarkable increase in capacitance can be explained by the increased surface area and micropore volume caused by the thiourea decomposition. At 10 A g^{-1}, the specific capacitance of pure CNF decreased to 84 F g^{-1}, remaining only 54.5% of that at 10 A g^{-1}. Meanwhile, for the N/S-CNF5, a capacitance of 149 F g^{-1} was found at 10 A g^{-1} showing a better retention capability (66.2%) compared to at 1 A g^{-1} (Fig. 7c). The enhancement of rate performance could be related to the fact that N/S-CNF5 has a better pore size distribution and especially high amount of N and S species than N/S-CNF2.5 and N/S-CNF10 [18, 47].

Figure 7d displays the specific capacitance values of CNFs obtained from the CV curves (10–200 mV s^{-1}). Clearly, the specific capacitances showed a decreasing trend as the scan rate increased. This is ascribed to the slower ion diffusion into the interior of the electrode, and the sample cannot resist to high scan rate, and a good capacitance rate retention of 84% was found for N/S-CNF5. In short, N/S-CNF5 was the best electrochemical performance with

respect to specific capacitance and rate retention, that can be used as an electrode. This is attributed to the combination of the effective double-layer capacitance resulting from a high specific surface with a synergistic effect of the hierarchical porous structure and microporosity as well as the pseudocapacitance resulting from N and S dual doping. The calculated electrode's specific capacitances under different scan rates and current densities are presented (Tables S1 and S2).

The CVs of the N/S-CNF5 electrode recorded at different scan rates (10, 50, and 100 mV s^{-1}) are presented in Fig. 8a. A quasi-rectangle curve was seen at 10 and 50 mV s^{-1}, and it became lightly twisted at a high scan rate of 100 mV s^{-1}. Meanwhile, no clear redox peaks were observed at any scan rates demonstrating that EDLC behavior was dominant at all. There was no noticeable change with the increase in scan rate, demonstrating its good rate performance and desirable capacitive property. Figure 8b shows the GCD curves of the N/S-CNF5 electrode at various current densities from 1 to 10 A g^{-1}. Isosceles triangle curves were observed, and the specific capacitance decreased with the increasing current density. This occurs because the electrolyte is confined by the micropores of the electrode, and the calculated specific capacitances are shown in Table S1.

To understand the capacitance performance of the N/S-CNF5 electrode in depth, the contribution of EDLC and pseudocapacitive effect were investigated quantitatively. For this reason, the kinetics and extensive charge storage mechanism of the N/S-
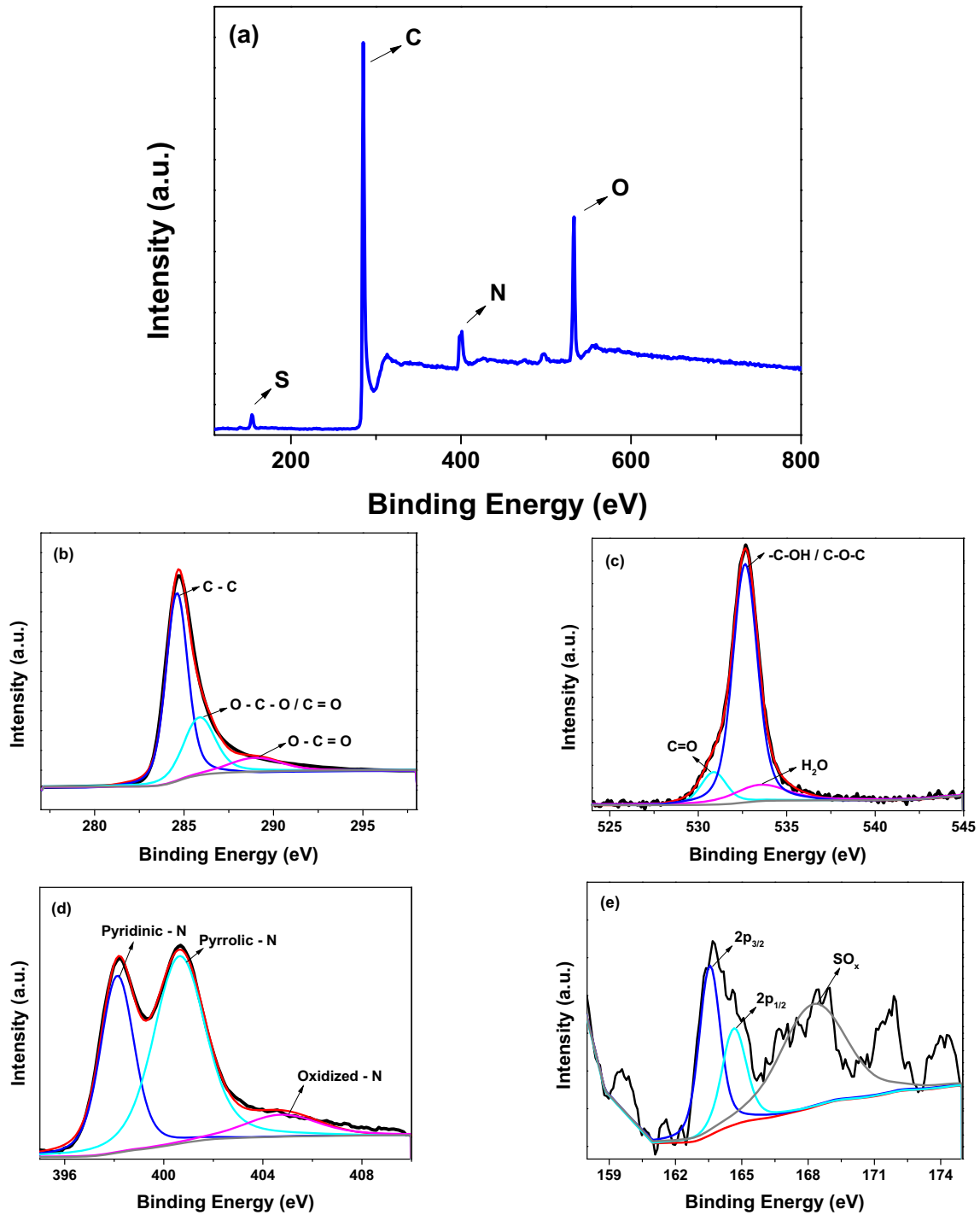
Fig. 6 **a** Wide scan XPS spectra of N/S-CNF5, **b** C 1 s, **c** O 1 s, **d** N 1 s, and **e** S 2p spectra

CNF5 sample were investigated using CV experiments in the three-electrode system. The current response at a particular potential (vs. Ag/AgCl) with different scan rates can be defined in the below formula [48].

$$i = av^b, \tag{5}$$

where i demonstrates the peak current (A), v shows the scanning speed (V/s), and a and b are the variable experimental parameters. The charge storage mechanism is defined according to the value of the kinetic
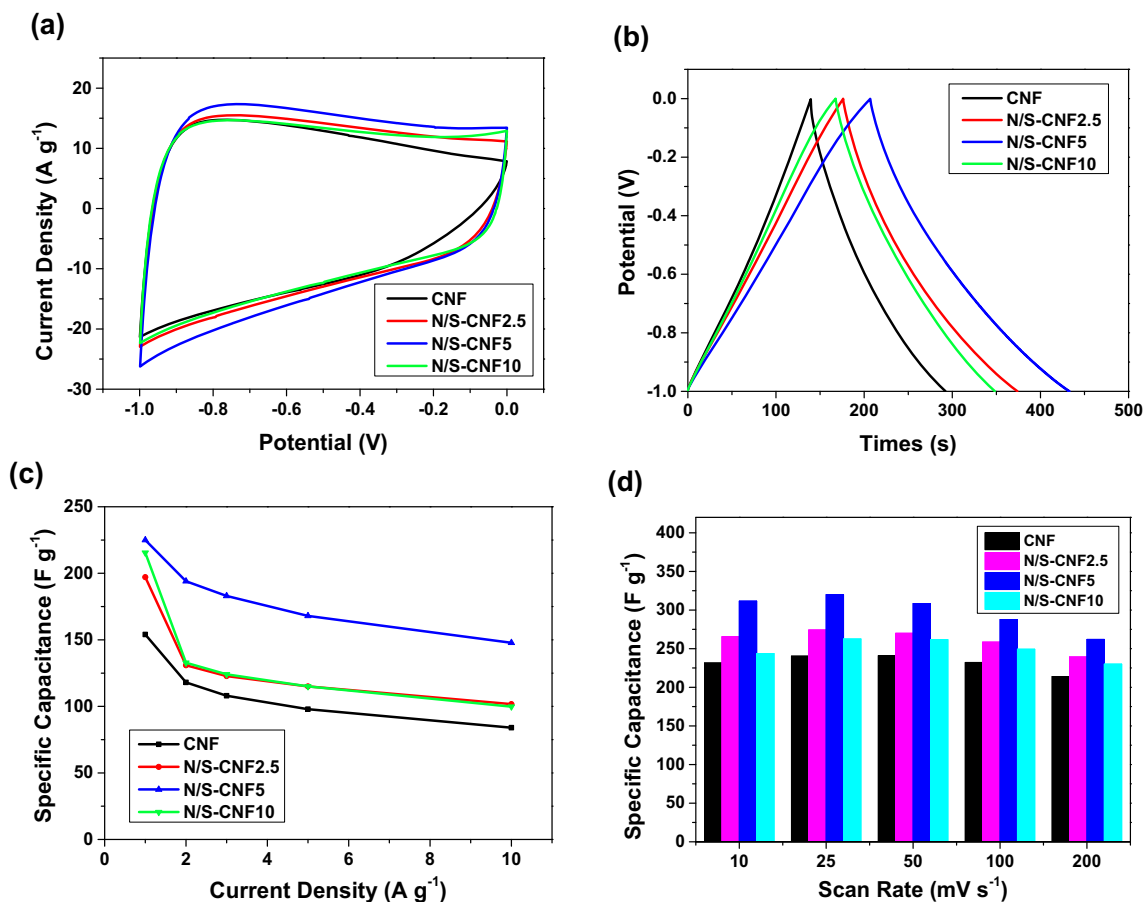
Fig. 7 Three electrode measurement results: **a** CV curves at 100 mV s^{-1}, **b** GCD curves at 1 A g^{-1}, the gravimetric-specific capacitance at several **c** current densities, and **d** scan rates

parameter b obtained from the slope of the diagram of log (i) versus log (v) (Fig. 8c).

Usually, when b approaches 0.5, it demonstrates that the electrode reaction is completely diffusion-controlled process, while b approaches 1, it means that the electrode reaction is capacitive charge storage. In Fig. 8d, the value of b for the N/S-CNF5 sample varied from 0.9 to 1.0 in the potential range of 0.1–0.8 V, demonstrating that the charge storage mechanism was almost controlled by surface and mostly capacitive.

In addition, the capacitive and diffusion-controlled contribution percentage can be further separated by Dunn et al. using the equation below [49].

$$i = k_1 v + k_2 v^{1/2}, \tag{6}$$

where $k_1 v$ is capacitive current, $k_2 v^{1/2}$ is diffusion-controlled current and i is total current contribution at a fixed potential (V). The above formulas can be explained as follows:

$$\frac{i}{v^{1/2}} = k_1 v^{1/2} + k_2, \tag{7}$$

The constant parameters k_1 and k_2 can be determined from the slope and intercept of the plot between $i/v^{1/2}$ and $v^{1/2}$. The curve of $i/v^{1/2}$ and $v^{1/2}$ at different constant potential (V) for charging and discharging is shown in Fig. 8e.

Figure 8f demonstrates the capacitive and diffusion-controlled contribution percentage calculated by Eq. (7). It has been shown that when increasing scan rates from 10 to 200 mV s^{-1}, the capacitive contribution ratio also increased from ∼ 80% to ∼ 95%. The diffusion-controlled contribution reduced due to the limitation of the electrolyte access at higher scan rates. The blue areas representing the capacitive contribution separated from the total current ($k_1 v$) at a scanning rate of 10 mV s^{-1} are shown in the CV plot in Fig. 8g. The gray color region indicates the diffusion-controlled contribution, which is 20.5%,

Fig. 8 **a** CV curves of N/S-CNF5 at different scan rates, **b** GCD curves of N/S-CNF5 at different current densities, **c** linear plot between log i vs. log v in different potentials, **d** b-values in different potentials, **e** linear plot between $iv^{-0.5}$ vs. $v^{0.5}$, **f** Histograms of the capacitive and diffusion-controlled contribution of N/S-CNF5 at different scan rates and **g** capacitive and diffusion-controlled contribution current of N/S-CNF5 at 10 mV s.$^{-1}$
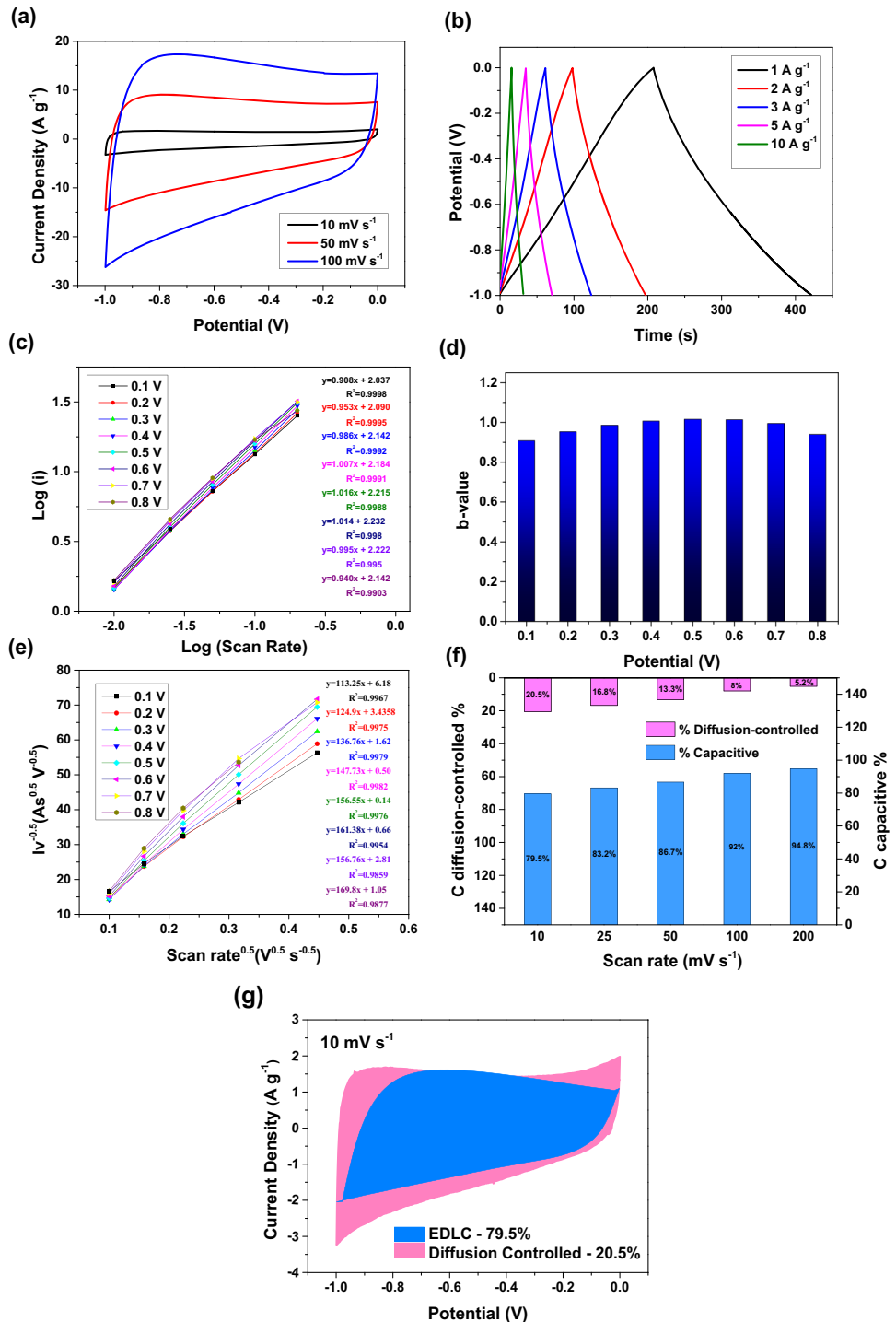
while the blue color region indicates the capacitive contribution, which is 79.5%. This analysis shows that charge storage was dominantly controlled by EDLC and partially controlled redox pseudocapacitance for all scan rates [50–53]. The high percentage of capacitive charge storage process may be due to ultra-high recyclability and good rate stability.

3.3 Electrochemical measurements conducted in a two-electrode system (supercapacitive tests)

A symmetric two-electrode cell was also constructed by using the as-fabricated electrodes as both positive and negative electrodes in order to further

demonstrate the practical application. The electrochemical results of the assembled two-electrode system are presented in Fig. 9. The CV plot of the N/S-CNF5//N/S-CNF5 compared to the pure CNF//CNF is shown at 10 mV s^{-1} and the integrated area was larger for N/S-CNF5//N/S-CNF5 (Fig. 9a). The gravimetric-specific capacitances of CNF//CNF and N/S-CNF5//N/S-CNF5 are shown in Fig. 9b at a scan rate of 10, 25, 50, 100, and 200 mV s^{-1}. The values of the N/S-CNF5//N/S-CNF5 were much better than that of the CNF//CNF and this enhanced supercapacitive performance is ascribed to the better textural properties and additional pseudocapacitive effects derived from heteroatom doping.

GCD curves are shown in Fig. 9c and it's clear that all plots were approximately linear with a slight bend which is related to the existence of the pseudocapacitive effect caused by the faradic reactions of heteroatom doping. Also, the IR drop was low which was also confirmed by the impedance result. The calculated specific capacitance of N/S-CNF5//N/S-CNF5 (Fig. 9d) reached up to 160 F g^{-1} at 1 A g^{-1}. The constant current charge–discharge tests of N/S-CNF5//N/S-CNF5 at different current densities from 1 to 5 A g^{-1} are shown in Fig. 9e. Almost symmetrical triangular curves were observed, demonstrating a fast and reversible mechanism with good electrochemical activity. The specific capacitance of the electrode was calculated from the GCD curve as shown in Fig. 9d. The specific capacitance values were found as 160, 144.5, 138.3, and 140 F g^{-1} at 1, 2, 3, and 5 A g^{-1}, respectively. During the measurement, the change of capacitance from 160 to 140 was seen as the current density varied from 1 to 5 A g^{-1}. The capacitance retention was 87.5% (Fig. 9e). The significant rate capability is due to the well-matched pore structure between the electrode and the electrolyte which are greater than those for reported heteroatom-doped carbon-based materials SCs (Table 3). K$^+$ and OH$^-$ ions could penetrate into the electrochemically active sites of the N/S-CNF5 electrode in an effective way due to its hierarchical interconnected pores even at a high current density (5 A g^{-1}).

Nyquist plots of CNFs consist of a vertical line at the low-frequency area and a semicircle at the high frequency by EIS analysis (Fig. 9f). The Rs values of pure CNF and N/S-CNF5 were 0.88 and 7.14Ω, indicating different ohmic resistances, respectively, in the EIS. N/S-CNF5 displayed a much smaller semi-circular diameter (Rct, 2.44Ω) than pure CNF (15.1Ω) as clearly depicted in Fig. 9f. These different values may probably result from the remarkable difference in the pore structures. In addition, N/S-CNF5 showed nearly perpendicular to the imaginary axis in the low-frequency region, which indicates that the electrolyte ions had the best diffusion ability in electrode structure and the straight line demonstrated the ideal capacitive behavior of electrode materials. The whole supercapacitive properties indicate that the conductive carbon nanofiber can be a promising electrode material to replace the other materials for SCs in near future.

The long cycle life of the N/S-CNF5//N/S-CNF5 was evaluated by using GCD cycles at 1 A g^{-1} (Fig. 9g). The device capacity was restored to 78.3% of its initial after 30 000 cycles at 1 A g^{-1}, confirming the significant electrochemical stability of the N/S-CNF5 electrode during the long-term electrochemical testing of the device (inset: GCD curves of the last ten cycles). Therefore, the above whole electrochemical results substantially proved that the N/S-CNF5 materials can be a great potential applied as an electrode for high-performance energy storage systems.

The device's energy and power density are significant parameters for energy storage systems and Fig. 9h shows the Ragone plot of N/S-CNF5//N/S-CNF5. The device delivered specific energy of 5.5 Wh kg^{-1} at a low specific power of 250 W kg^{-1}. Even at a high a specific power of 1250 W kg^{-1}, the SC can still sustain efficiently its specific energy of 4.9 Wh kg^{-1}, which are competitive with those of several recently reported heteroatom-doped carbon-based materials SC devices (Table 3). The calculated electrochemical results of N/S-CNF5//N/S-CNF5 and CNF//CNF are shown in Table 4.

4 Conclusion

In summary, we suggested an attractive synthesis of approach for the fabrication of PAN-based heteroatom (nitrogen and sulfur) dual-doped CNFs with thiourea addition by electrospinning and carbonization process. The results represent the following: (i) Thiourea was significant to obtain unique pore architecture and surface chemistry. What's more, the quantities of N and S species and pore structures were well tuned by different amounts of thiourea

Fig. 9 Symmetric coin-cell SC performance of CNF//CNF and N/S-CNF5//N/S-CNF5 **a** CV curve at 10 m V^{-1}, **b** gravimetric-specific capacitances at different scan rates from 10 to 200 m V^{-1}, **c** GCD curves at several current densities at 1 A g^{-1}, **d** gravimetric-specific capacitances at different current densities, **e** GCD curves of N/S-CNF5//N/S-CNF5 at several current densities from 1 to 5 A g^{-1} **f** impedance plot, **g** long-term cycle test of N/S-CNF5//N/S-CNF5 device over 30 000 cycles at 1 A g^{-1} and **h** Ragone plots
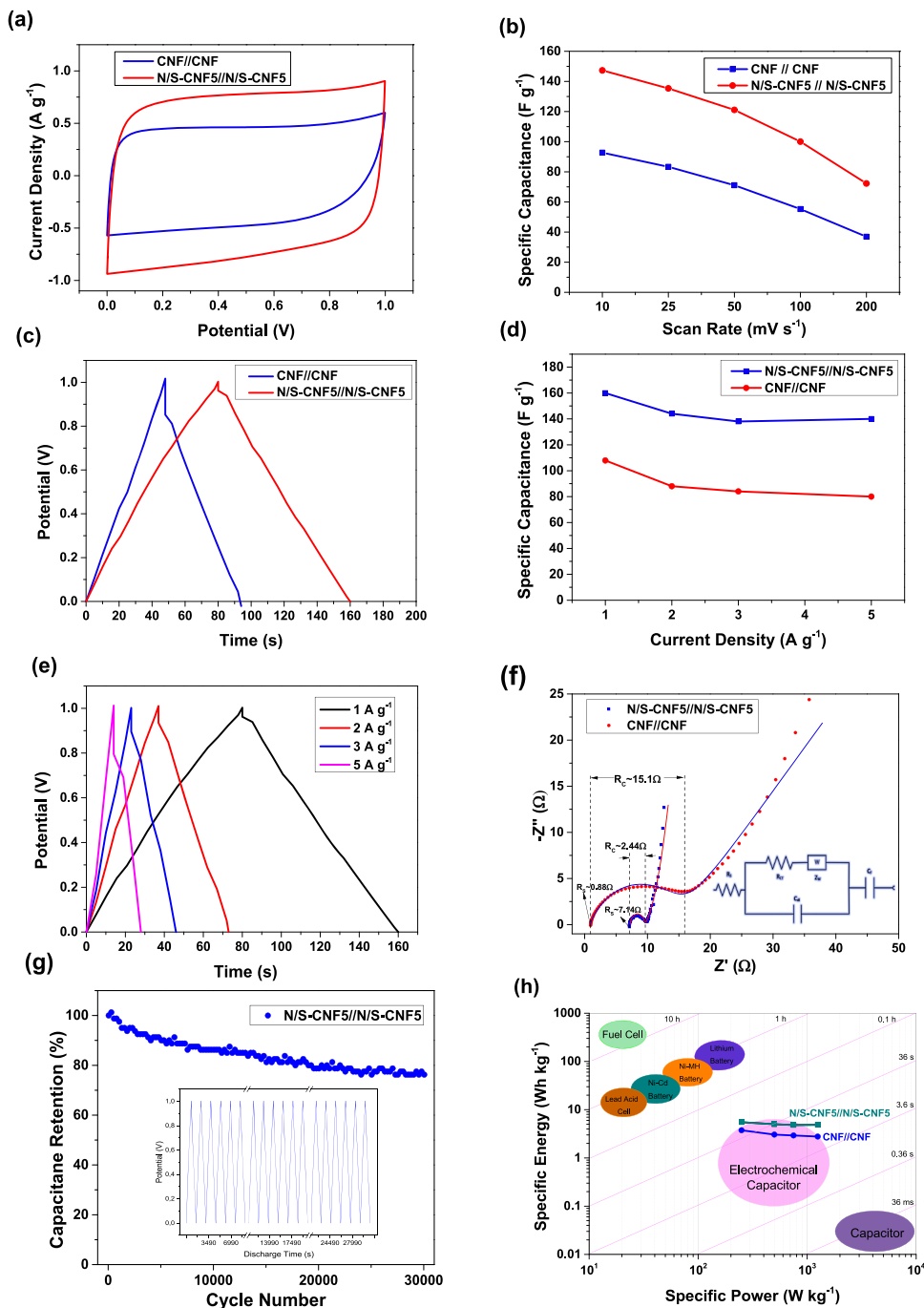
addition; (ii) N/S-CNF5 possessed a larger pore volume (0.325 cm^3 g^{-1}) and a higher specific surface area (144.2 m^2 g^{-1}) with rich heteroatom contents including nitrogen (4.66%), oxygen (12.78%), and sulfur (0.11%). Hierarchical structure with high porosity and a large pore volume, thereby creating more efficient adsorption sites for ions transportation of the electrolyte, consequently improved the ionic conductivity; (iii) the specific capacitance of the N/S-CNF5 electrode was 224 F g^{-1} at 1 A g^{-1} and good capacitance retention of 87.5% was found at 5 A g^{-1}, and (iv) the N/S-CNF5//N/S-CNF5 symmetric SC exhibited high specific energy of 5.5 to 4.9 Wh kg^{-1} and specific power from 250 to 1250 W kg^{-1} with enhanced cycling stability (78.3%). As a consequence, this increase in capacitance observed in the N/S-CNF5 sample was ascribed to the addition of thiourea which contributes in increase in "N" and

Table 1 BET specific surface area and pore parameters of CNF, N/S-CNF2.5, N/S-CNF5, and N/S-CNF10 electrodes

Sample	S_{BET} (m^2g^{-1})	V_{Total} (cm^3g^{-1})	V_{Meso}^a (cm^3g^{-1})	V_{Micro}^b (cm^3g^{-1})	D_{av}^c (nm)
CNF	62.8	0.153	0.135	0.0188	7.78
N/S-CNF2.5	113.46	0.247	0.214	0.0332	7.23
N/S-CNF5	144.2	0.325	0.276	0.0497	7.35
N/S-CNF10	35.35	0.179	0.160	0.019	17.2

^{a}Data obtained from BJH at 1.7–300 nm

^{b}Data obtained from Horvarth-Kawazoe at 0.6–1.7 nm

^{c}Desorption average pore size (4 V/A by BET)

Table 2 Summary of the elemental composition obtained from XPS peak analysis

Sample	Surface element (at.%)				N 1 s (at.%)			S 2p (at.%)			O 1 s (at.%)		
	C	O	N	S	N1	N2	N3	S1	S2	S3	O1	O2	O3
N/S-CNF5	82.45	12.78	4.66	0.11	43.57	46.50	9.93	38.39	31	30.61	57.9	13.76	28.34

Table 3 Comparison of the device parameters of N/S-CNF in our work and some heteroatom-doped carbon electrodes reported in the literature

References	Electrode	Specific capacitance	Energy and power density	Electrolyte	Potential	Stability
Our work	**N/S-CNF5**	**160 F g^{-1}** **1 A g^{-1}**	**5.5 Wh kg^{-1}** **250 W kg^{-1}**	**6 M KOH**	**0–1 V**	**78.3% 30 000 cycles**
[34]	NSCF	80 F g^{-1} 0.5 A g^{-1}	Not reported	6 M KOH	0–1 V	98% 5 000 cycles
[54]	N/S-MC	125 F g^{-1} 0.5 A g^{-1}	Not reported	6 M KOH	0–1.2 V	90.6% 3 000 cycles
[55]	SUMBC	140 F g^{-1} 0.5 A g^{-1}	5.41 Wh kg^{-1} 500 W kg^{-1}	PVA/KOH	0–1 V	87% 5000 cycles
[56]	PHCNF30	152.1 F g^{-1} 1 A g^{-1}	5.28 Wh kg^{-1} 500 W kg^{-1}	2 M KOH	0–1 V	92.33% 10 000 cycles
[57]	N,S-CLPACF	170 F g^{-1} 0.2 A g^{-1}	4.7 Wh kg^{-1} 1.2 kW kg^{-1}	6 M KOH	0–1 V	98% 10 000 cycles
[58]	Co$_2$P$_2$O$_7$@N–C2	384 F g^{-1} 10 mV s^{-1}	5.68 Wh kg^{-1} 325 W kg^{-1}	6 M KOH	0–1.3 V	76.7% 10 000 cycles

Table 4 Supercapacitive energy storage values of CNF//CNF and N/S-CNF5//N/S-CNF5 calculated at various current densities

Current density (A g^{-1})	CNF//CNF			N/S-CNF5//N/S-CNF5		
	Capacitance (F g^{-1})	Specific energy (Wh kg^{-1})	Specific power (W kg^{-1})	Capacitance (F g^{-1})	Specific energy (Wh kg^{-1})	Specific power (W kg^{-1})
1	108	3.75	250	160	5.5	250
2	87.5	3.1	500	144.5	5	500
3	84.2	2.93	750	138.3	4.8	750
5	79.6	2.78	1250	140	4.86	1250

"S"-containing functional groups, enhancement in graphitization, rich active heteroatom contents, small charge-transfer resistance, and large ion diffusion than that of pure CNF. This type of material could be used in next energy storage applications.

Author contributions

BÜ contributed to experiments, electrochemical tests, graphical drawing, data analysis, and software. HA contributed to design of the research, materials characterization, electrochemical analysis, and writing, ÜK contributed to investigation, conceptualization, writing the original draft and editing, and materials characterization; and SNK contributed to the guidance for the whole research, review, and supervision.

Funding

Data availability

All data generated or analyzed during this research are included in this article and in its supplementary file.

Declarations

Competing interests The authors declare that they have no conflict of financial interests or personal relationships that could have appeared to influence the work reported in this paper.

Supplementary Information: The online version contains supplementary material available at https://doi.org/10.1007/s10854-023-09843-4.

References

1. E. Harputlu, C. Gecgel, Fabrication of LaFeO3/g-C3N4@reduced graphene oxide 3-dimensional nanostructure supercapacitor. J. Mater. Sci. Mater. Electron. **33**, 25687–25703 (2022). https://doi.org/10.1007/s10854-022-09264-9

2. M.C. Ribadeneyra, L. Grogan, H. Au, P. Schlee, S. Herou, T. Neville, P.L. Cullen, M.D.R. Kok, O. Hosseinaei, S. Danielsson, P. Tomani, M.M. Titirici, D.J.L. Brett, P.R. Shearing, R. Jervis, A.B. Jorge, Lignin-derived electrospun freestanding carbons as alternative electrodes for redox flow batteries. Carbon NY **157**, 847–856 (2020). https://doi.org/10.1016/j.carbon.2019.11.015

3. J. Liang, H. Zhao, L. Yue, G. Fan, T. Li, S. Lu, G. Chen, S. Gao, A.M. Asiri, X. Sun, Recent advances in electrospun nanofibers for supercapacitors. J. Mater. Chem. A (2020). https://doi.org/10.1039/d0ta05100d

4. E. Ceylan Cengiz, Z. Erdol, B. Sakar, A. Aslan, A. Ata, O. Ozturk, R. Demir-Cakan, Investigation of the effect of using Al2O3–nafion barrier on room-temperature Na–S batteries. J. Phys. Chem. C **121**, 15120–15126 (2017). https://doi.org/10.1021/acs.jpcc.7b04711

5. S. Hussain, X. Yang, M.K. Aslam, A. Shaheen, M.S. Javed, N. Aslam, B. Aslam, G. Liu, G. Qiao, Robust TiN nanoparticles polysulfide anchor for Li–S storage and diffusion pathways using first principle calculations. Chem. Eng. J. **391**, 123595 (2020). https://doi.org/10.1016/j.cej.2019.123595

6. S. Hussain, A.J. Khan, M. Arshad, M.S. Javed, A. Ahmad, S.S. Shah, M.R. Khan, S. Akram, S. Ali, Z.A. ALOthman, G. Liu, Charge storage in binder-free 2D-hexagonal CoMoO4 nanosheets as a redox active material for pseudocapacitors. Ceram. Int. **47**, 8659–8667 (2021). https://doi.org/10.1016/j.ceramint.2020.11.237

7. R. Singhal, V. Kalra, Using common salt to impart pseudocapacitive functionalities to carbon nanofibers. J. Mater. Chem. A **3**, 377–385 (2015). https://doi.org/10.1039/c4ta05121a

8. M. Tahir, C. Cao, N. Mahmood, F.K. Butt, A. Mahmood, F. Idrees, S. Hussain, M. Tanveer, Z. Ali, I. Aslam, Multifunctional g-C3N4 nanofibers: a template-free fabrication and enhanced optical, electrochemical, and photocatalyst properties. ACS Appl. Mater. Interfaces **6**, 1258–1265 (2014). https://doi.org/10.1021/am405076b

9. G. Wu, P. Tan, X. Wu, L. Peng, H. Cheng, C.-F. Wang, W. Chen, Z. Yu, S. Chen, High-performance wearable micro-supercapacitors based on microfluidic-directed nitrogen-doped graphene fiber electrodes. Adv. Funct. Mater. **27**, 1702493 (2017). https://doi.org/10.1002/adfm.201702493

10. Y. Liu, J. Zhou, L. Chen, P. Zhang, W. Fu, H. Zhao, Y. Ma, X. Pan, Z. Zhang, W. Han, Highly flexible freestanding porous carbon nanofibers for electrodes materials of high-performance all-carbon supercapacitors. ACS Appl. Mater. Interfaces **7**, 23515–23520 (2015)

11. H. Wang, W. Wang, H. Wang, X. Jin, H. Niu, H. Wang, H. Zhou, T. Lin, High performance supercapacitor electrode materials from electrospun carbon nanofibers in situ activated by high decomposition temperature polymer. ACS Appl. Energy Mater. **1**, 431–439 (2018)

12. Y. Mao, H. Duan, B. Xu, L. Zhang, Y. Hu, C. Zhao, Z. Wang, L. Chen, Y. Yang, Lithium storage in nitrogen-rich mesoporous carbon materials. Energy Environ. Sci. **5**, 7950–7955 (2012). https://doi.org/10.1039/c2ee21817h

13. U. Kurtan, Uniformly decorated nanocubes in carbon nanofibers for a supercapacitor with ultrahigh cyclability and stability. J. Electron. Mater. **51**, 5159–5168 (2022). https://doi.org/10.1007/s11664-022-09729-x

14. X. Li, L. Zhao, T. He, M. Zhang, Z. Wang, B. Zhang, X. Weng, Highly conductive, hierarchical porous ultra-fine carbon fibers derived from polyacrylonitrile/polymethylmethacrylate/needle coke as binder-free electrodes for high-performance supercapacitors. J. Power Sources **521**, 230943 (2022). https://doi.org/10.1016/j.jpowsour.2021.230943

15. Y. Altin, A. Celik Bedeloglu, Polyacrylonitrile/polyvinyl alcohol-based porous carbon nanofiber electrodes for supercapacitor applications. Int. J. Energy Res. **45**, 16497–16510 (2021). https://doi.org/10.1002/er.6896

16. B.H. Kim, K.S. Yang, J.P. Ferraris, Highly conductive, mesoporous carbon nanofiber web as electrode material for high-performance supercapacitors. Electrochim. Acta **75**, 325–331 (2012). https://doi.org/10.1016/j.electacta.2012.05.004

17. F. Miao, C. Shao, X. Li, K. Wang, Y. Liu, Flexible solid-state supercapacitors based on freestanding nitrogen-doped porous carbon nanofibers derived from electrospun polyacrylonitrile@polyaniline nanofibers. J. Mater. Chem. A **4**, 4180–4187 (2016). https://doi.org/10.1039/c6ta00015k

18. M. Chen, T.H. Le, Y. Zhou, F. Kang, Y. Yang, Thiourea-induced N/S dual-doped hierarchical porous carbon nanofibers for high-performance lithium-ion capacitors. ACS Appl. Energy Mater. **3**, 1653–1664 (2020). https://doi.org/10.1021/acsaem.9b02157

19. M.W. Ahmad, S. Anand, B. Dey, A. Fatima, D.J. Yang, A. Choudhury, N/P/O/S heteroatom-doped porous carbon nanofiber mats derived from a polyacrylonitrile/l-Cysteine/P2O5 precursor for flexible electrochemical supercapacitors. ACS Appl. Energy Mater. (2021). https://doi.org/10.1021/acsaem.1c01790

20. Y. Li, G. Zhu, H. Huang, M. Xu, T. Lu, L. Pan, A N, S dual doping strategy: Via electrospinning to prepare hierarchically porous carbon polyhedra embedded carbon nanofibers for flexible supercapacitors. J. Mater. Chem. A **7**, 9040–9050 (2019). https://doi.org/10.1039/c8ta12246f

21. Ü. Kurtan, Carbon nanofibers fabricated from electrospun nano-sized boron oxide/polyacrylonitrile nanofibers as electrode for supercapacitors. Sak. Univ. J. Sci. **25**, 1180–1188 (2021). https://doi.org/10.16984/saufenbilder.877089

22. M. Demir, B. Ashourirad, J.H. Mugumya, S.K. Saraswat, H.M. El-Kaderi, R.B. Gupta, Nitrogen and oxygen dual-doped porous carbons prepared from pea protein as electrode materials for high performance supercapacitors. Int. J. Hydrogen Energy **43**, 18549–18558 (2018). https://doi.org/10.1016/j.ijhydene.2018.03.220

23. Q. Wei, F. Xiong, S. Tan, L. Huang, E.H. Lan, B. Dunn, L. Mai, Porous one-dimensional nanomaterials: design, fabrication and applications in electrochemical energy storage. Adv. Mater. (2017). https://doi.org/10.1002/adma.201602300

24. B. Zhang, F. Kang, J.M. Tarascon, J.K. Kim, Recent advances in electrospun carbon nanofibers and their application in electrochemical energy storage. Prog. Mater. Sci. **76**, 319–380 (2016). https://doi.org/10.1016/j.pmatsci.2015.08.002

25. U. Kurtan, H. Aydın, Introducing organic metallic salts to enhance capacitive energy storage of carbon nanofibers. J. Energy Storage **42**, 103016 (2021). https://doi.org/10.1016/j.est.2021.103016

26. M. Fukuhara, T. Kuroda, F. Hasegawa, T. Hashida, M. Takeda, N. Fujima, M. Morita, T. Nakatani, Amorphous cellulose nanofiber supercapacitors. Sci. Rep. **11**, 1–7 (2021). https://doi.org/10.1038/s41598-021-85901-3

27. X.Y. Li, Y. Yan, B. Zhang, T.J. Bai, Z.Z. Wang, T.S. He, PAN-derived electrospun nanofibers for supercapacitor applications: ongoing approaches and challenges. J. Mater. Sci. (2021). https://doi.org/10.1007/s10853-021-05939-6

28. L.F. Chen, Y. Lu, L. Yu, X.W. Lou, Designed formation of hollow particle-based nitrogen-doped carbon nanofibers for high-performance supercapacitors. Energy Environ. Sci. **10**, 1777–1783 (2017). https://doi.org/10.1039/c7ee00488e

29. S.B. Kale, M.A. Mahadadalkar, C.H. Kim, Y.A. Kim, M.S. Jayswal, K.S. Yang, B.B. Kale, N-Enriched carbon nanofibers for high energy density supercapacitors and Li-ion batteries. RSC Adv. **9**, 36075–36081 (2019). https://doi.org/10.1039/c9ra05780c

30. G. Hasegawa, M. Aoki, K. Kanamori, K. Nakanishi, T. Hanada, K. Tadanaga, Monolithic electrode for electric double-layer capacitors based on macro/meso/microporous S-containing activated carbon with high surface area. J. Mater. Chem. **21**, 2060–2063 (2011). https://doi.org/10.1039/c0jm03793a

31. N. Parveen, M.O. Ansari, S.A. Ansari, M.H. Cho, Simultaneous sulfur doping and exfoliation of graphene from graphite using an electrochemical method for supercapacitor electrode materials. J. Mater. Chem. A **4**, 233–240 (2016)

32. W. Zong, F. Lai, G. He, J. Feng, W. Wang, R. Lian, Y.E. Miao, G.C. Wang, I.P. Parkin, T. Liu, Sulfur-deficient bismuth sulfide/nitrogen-doped carbon nanofibers as advanced free-standing electrode for asymmetric supercapacitors. Small **14**, 1–9 (2018). https://doi.org/10.1002/smll.201801562

33. Y. Long, X. Qian, N. Guo, Improved electrochemical performance of mesoporous carbon via N / S doping. J. Solid State Electrochem. (2022). https://doi.org/10.1007/s10008-022-05145-7

34. W. Lei, H. Zhang, D. Liu, L. Lin, Fabrication of nitrogen and sulfur co-doped carbon nanofibers with three-dimensional architecture for high performance supercapacitors. Appl. Surf. Sci. **495**, 143572 (2019). https://doi.org/10.1016/j.apsusc.2019.143572

35. M. Wang, H. Liu, D.D. Zhai, X.Y. Chen, Z.J. Zhang, In-situ synthesis of highly nitrogen, sulfur co-doped carbon nanosheets from melamine-formaldehyde-thiourea resin with improved cycling stability and energy density for supercapacitors. J. Power Sources **416**, 79–88 (2019). https://doi.org/10.1016/j.jpowsour.2019.01.092

36. S. Zhao, H. Wu, Y. Li, Q. Li, J. Zhou, X. Yu, H. Chen, K. Tao, L. Han, Core-shell assembly of carbon nanofibers and a 2D conductive metal-organic framework as a flexible free-standing membrane for high-performance supercapacitors. Inorg. Chem. Front. **6**, 1824–1830 (2019). https://doi.org/10.1039/c9qi00390h

37. J.C. Lee, J.Y. Kim, W.H. Joo, D. Hong, S.H. Oh, B. Kim, G.D. Lee, M. Kim, J. Oh, Y.C. Joo, Thermodynamically driven self-formation of copper-embedded nitrogen-doped carbon nanofiber catalysts for a cascade electroreduction of carbon dioxide to ethylene. J. Mater. Chem. A **8**, 11632–11641 (2020)

38. Y. Lv, L. Ding, X. Wu, N. Guo, J. Guo, S. Hou, F. Tong, D. Jia, H. Zhang, Coal-based 3D hierarchical porous carbon aerogels for high performance and super-long life supercapacitors. Sci. Rep. **10**, 1–11 (2020). https://doi.org/10.1038/s41598-020-64020-5

39. H. Aydın, U. Kurtan, M. Demir, S. Karakuş, Synthesis and application of a self-standing zirconia-based carbon nanofiber in a supercapacitor. Energy Fuels (2022). https://doi.org/10.1021/acs.energyfuels.1c04208

40. A. Ganguly, S. Sharma, P. Papakonstantinou, J. Hamilton, Probing the thermal deoxygenation of graphene oxide using high-resolution in situ X-ray-based spectroscopies. J. Phys. Chem. C **115**, 17009–17019 (2011)

41. V.R. Moreira, Y.A.R. Lebron, M.M. da Silva, L.V. de Souza Santos, R.S. Jacob, C.K.B. de Vasconcelos, M.M. Viana, Graphene oxide in the remediation of norfloxacin from aqueous matrix: simultaneous adsorption and degradation process. Environ. Sci. Pollut. Res. **27**, 34513–34528 (2020)

42. N. Díez, A. Śliwak, S. Gryglewicz, B. Grzyb, G. Gryglewicz, Enhanced reduction of graphene oxide by high-pressure hydrothermal treatment. Rsc Adv. **5**, 81831–81837 (2015)

43. D. Wei, Y. Liu, Y. Wang, H. Zhang, L. Huang, G. Yu, Synthesis of N-doped graphene by chemical vapor deposition and its electrical properties. Nano Lett. **9**, 1752–1758 (2009)

44. B.J. Matsoso, K. Ranganathan, B.K. Mutuma, T. Lerotholi, G. Jones, N.J. Coville, Time-dependent evolution of the nitrogen configurations in N-doped graphene films. RSC Adv. **6**, 106914–106920 (2016). https://doi.org/10.1039/C6RA24094A

45. G. Zhou, E. Paek, G.S. Hwang, A. Manthiram, Long-life Li/polysulphide batteries with high sulphur loading enabled by lightweight three-dimensional nitrogen/sulphur-codoped graphene sponge. Nat. Commun. **6**, 1–11 (2015)

46. H. Gao, Z. Liu, L. Song, W. Guo, W. Gao, L. Ci, A. Rao, W. Quan, R. Vajtai, P.M. Ajayan, Synthesis of S-doped graphene by liquid precursor. Nanotechnology **23**, 275605 (2012)

47. Q. Jiang, X. Pang, S. Geng, Y. Zhao, X. Wang, H. Qin, B. Liu, J. Zhou, T. Zhou, Simultaneous cross-linking and pore-forming electrospun carbon nanofibers towards high capacitive performance. Appl. Surf. Sci. **479**, 128–136 (2019). https://doi.org/10.1016/j.apsusc.2019.02.077

48. S. Gharehkhani, S.F.S. Shirazi, S.P. Jahromi, M. Sookhakian, S. Baradaran, H. Yarmand, A.A. Oshkour, S.N. Kazi, W.J. Basirun, Spongy nitrogen-doped activated carbonaceous hybrid derived from biomass material/graphene oxide for supercapacitor electrodes. Rsc Adv. **5**, 40505–40513 (2015)

49. J. Wang, J. Polleux, J. Lim, B. Dunn, Pseudocapacitive contributions to electrochemical energy storage in TiO 2 (anatase) nanoparticles. J. Phys. Chem. C **111**, 14925–14931 (2007). https://doi.org/10.1021/jp074464w

50. S. Bhoyate, P.K. Kahol, B. Sapkota, S.R. Mishra, F. Perez, R.K. Gupta, Polystyrene activated linear tube carbon nanofiber for durable and high-performance supercapacitors. Surf. Coatings Technol. **345**, 113–122 (2018). https://doi.org/10.1016/j.surfcoat.2018.04.026

51. L. Saleh Ghadimi, N. Arsalani, A.G. Tabrizi, A. Mohammadi, I. Ahadzadeh, Novel nanocomposite of MnFe2O4 and nitrogen-doped carbon from polyaniline carbonization as electrode material for symmetric ultra-stable supercapacitor. Electrochim. Acta **282**, 116–127 (2018). https://doi.org/10.1016/j.electacta.2018.05.160

52. T. Islam, M.M. Hasan, S.S. Shah, M.R. Karim, F.S. Al-Mubaddel, M.H. Zahir, M.A. Dar, M.D. Hossain, M.A. Aziz, A.J.S. Ahammad, High yield activated porous coal carbon nanosheets from Boropukuria coal mine as supercapacitor material: Investigation of the charge storing mechanism at the interfacial region. J. Energy Storage **32**, 101908 (2020). https://doi.org/10.1016/j.est.2020.101908

53. W. Chen, X. Zhang, L.E. Mo, Y. Zhang, S. Chen, X. Zhang, L. Hu, NiCo2S4 quantum dots with high redox reactivity for hybrid supercapacitors. Chem. Eng. J. **388**, 124109 (2020). https://doi.org/10.1016/j.cej.2020.124109

54. Y.L. Xie, Q.N. Guo, Improved electrochemical performance of mesoporous carbon via N/S doping. J. Solid State Electrochem. (2022). https://doi.org/10.1007/s10008-022-05145-7

55. Q. Deng, S.C. Abbas, Z. Li, J. Lv, X. Ma, S. Cao, Y. Ni, W. Zhao, Chemically modified self-doped biocarbon via novel sulfonation assisted sacrificial template method for high performance flexible all solid-state supercapacitor. J. Colloid Interface Sci. **574**, 33–42 (2020). https://doi.org/10.1016/j.jcis.2020.04.029

56. J.G. Kim, H.C. Kim, N.D. Kim, M.S. Khil, N-doped hierarchical porous hollow carbon nanofibers based on PAN/PVP@SAN structure for high performance supercapacitor. Compos. Part B Eng. (2020). https://doi.org/10.1016/j.compositesb.2020.107825

57. X. Li, X. Du, Y. Li, X. Tian, H. Zheng, X. Li, Flexible and cross-linked N, S co-doped carbon nanofiber nonwovens derived from coal liquefaction residue for high performance supercapacitors. J. Mater. Sci. **57**, 9357–9369 (2022). https://doi.org/10.1007/s10853-022-07215-7

58. H. Aydın, Ü. Kurtan, B. Üstün, S.N. Koç, One-pot synthesis of cobalt pyrophosphate nanoparticles combined with mesoporous carbon for asymmetric supercapacitors. Mater. Chem. Phys. **290**, 126392 (2022). https://doi.org/10.1016/j.matchemphys.2022.126392